Experimental analysis of the hydrodynamic performance of an industrial-scale cross-flow sieve tray

Vishwakarma, V.; Abdul Haq, S.; Schleicher, E.; Schubert, M.; Hampel, U.;

Originally published:

August 2021

Chemical Engineering Research and Design 174(2021), 294-306

DOI: https://doi.org/10.1016/j.cherd.2021.07.026

Perma-Link to Publication Repository of HZDR:

https://www.hzdr.de/publications/Publ-32284

Experimental analysis of the hydrodynamic performance of an industrial-scale cross-flow sieve tray

Journal:	*AIChE Journal*
Manuscript ID	AIChE-21-23652
Wiley - Manuscript type:	Research Article
Date Submitted by the Author:	09-Feb-2021
Complete List of Authors:	Vishwakarma, Vineet; Helmholtz-Zentrum Dresden-Rossendorf, Institute of Fluid Dynamics Haq, Shadrukh; Helmholtz-Zentrum Dresden-Rossendorf, Institute of Fluid Dynamics Schleicher, Eckhard; Helmholtz-Zentrum Dresden-Rossendorf, Institute of Fluid Dynamics Schubert, Markus; Helmholtz-Zentrum Dresden-Rossendorf, Institute of Fluid Dynamics Hampel, Uwe; Helmholtz-Zentrum Dresden-Rossendorf, Institute of Fluid Dynamics
Keywords:	column tray, hydrodynamics, effective froth height, 3D liquid holdup, tracer-response analysis

Experimental analysis of the hydrodynamic performance of an industrial-scale cross-flow sieve tray

Vineet Vishwakarma[a,b,*], Shadrukh Abdul Haq[a], Eckhard Schleicher[a], Markus Schubert[a,*], and Uwe Hampel[a,b]

[a]Institute of Fluid Dynamics, Helmholtz-Zentrum Dresden-Rossendorf, Bautzner Landstraße 400, 01328 Dresden, Germany

[b]Chair of Imaging Techniques in Energy and Process Engineering, Technische Universität Dresden, 01062 Dresden, Germany

*Corresponding authors: m.schubert@hzdr.de (M. Schubert)

v.vishwakarma@hzdr.de (V. Vishwakarma)

Abstract: This work reports the hydrodynamic description of a large-scale sieve tray equipped in an air/water column mockup. The test tray accommodates a multi-probe flow profiler for simultaneous conductivity measurements. 3D liquid holdup distribution, liquid residence time distribution and effective froth height distribution are obtained at high spatiotemporal resolution for several gas and liquid loadings. The liquid flow and mixing patterns are visualized via tracer-based experiments. The methodologies used for acquiring these distributions are discussed in this work. Thorough examination of the processed experimental data reveals the hydrodynamic characteristics of an operational sieve tray for the studied loadings.

Topic: Transport Phenomena and Fluid Mechanics

Keywords: column tray, hydrodynamics, effective froth height, 3D liquid holdup, tracer-response analysis.

1. Introduction

Industrial tray columns are omnipresent in distillation, absorption and other thermal separation processes.[1,2] High energy demand and unavailability of an equivalent industrially-viable alternative have led to continuous academic and industrial interest towards performance optimization and prediction of tray columns.[3-7] The prevailing hydrodynamics in these columns significantly impact their separation performance.[8-10] As these columns are cascades of geometrically and functionally similar trays,[11] a complete understanding of tray hydrodynamics is essential for precisely accounting their effects on the tray efficiency (especially during the design phase).[4,6,12-15] Subsequently, the tray and column performances can be improved through hydrodynamic optimizations via design modifications leading to more cost- and energy-efficient processes.[1,8]

In the present context, the term 'hydrodynamics' refers to liquid or gas holdup, pressure drop, clear liquid height, froth height, liquid entrainment, weeping and residence time distribution (RTD), and so forth.[14] Most trivial measurements are those of pressure drop and clear liquid height (via U-tube manometer), visual froth height, and wept and entrained liquid collection.[3] On the other hand, the distributions of effective froth height, liquid holdup and residence time over the tray bubbling area are difficult to obtain, because of the chaotic and three-dimensional (3D) nature of the two-phase cross-flow.[12,13] γ-ray densitometry technique[16-21] has been extensively used to determine liquid holdup at selective locations on small trays and in rectangular tray columns. The application of γ-ray computed tomography in circular tray columns has been limited to process monitoring and troubleshooting assignments.[22-25] Furthermore, flow non-idealities or maldistribution in the liquid phase (with respect to a desirable uniform and unidirectional flow) are identified via measurements of residence time distribution (RTD) and velocity patterns.[26] Such information is usually retrieved from the two-phase dispersion above the tray through flow monitoring of a liquid tracer using camera techniques (photographic[27] and infrared[28]) and (multiple) point measurements (fiber-optic probes,[29] conductivity probes,[30] and wire-mesh sensor[31]). Other studies relying on point measurements used

thermocouples,[32] strain gauge probes,[33] thermometers,[34] and hot film anemometer.[35] Although these techniques were successful in identifying gross maldistribution, the camera techniques can provide flow patterns near the dispersion surface only, whereas the point measurements suffer from a variety of challenges such as high intrusiveness, low spatial resolution, complex calibration scheme, to name only a few. Thorough reviews of these techniques are available elsewhere.[11,36]

Apparently, the existing experimental studies lack a complete 3D hydrodynamic description of large-scale sieve trays. To address this limitation, CFD models have been used complementarily since last two decades,[25] however, they also depend on the availability of high-quality experimental data for validation. Hitherto, available data for CFD model validation include pressure drop, clear liquid height and low-resolution RTD profiles only.[11] However, accurate predictions of the tray performance and improved benchmarking of the CFD models indispensably require extensive hydrodynamic data based on advanced measurement techniques.

The present work reports the first in-depth hydrodynamic characterization of a large-scale sieve tray using a recently-introduced 'advanced multiplex flow profiler'.[36-39] Effective froth height distribution, 3D liquid holdup distribution, and liquid RTD and related parameters (based on tracer-response analysis) are obtained at high spatiotemporal resolution for several gas and liquid loadings. The methodologies used for deriving these parameter distributions are described here. The underlying trends in these distributions and their physical explanation are also reported in this work.

2. Experimental setup and instrumentation

2.1 Sieve tray column mock-up

Fig. 1 shows a schematic diagram of column mockup, auxiliary equipment and instrumentation. The column (800 mm ID) consists of three flange-mounted segments that are 860 mm, 375 mm, and 735 mm from bottom to top, respectively. Each intersection between the segments holds a 15 mm thick

PMMA sieve tray with 3052 holes of 5 mm diameter (i.e., equivalent to 13.55% fractional free area). The effective spacing between the trays is 365 mm. Further specifications of the facility are summarized in Table 1.

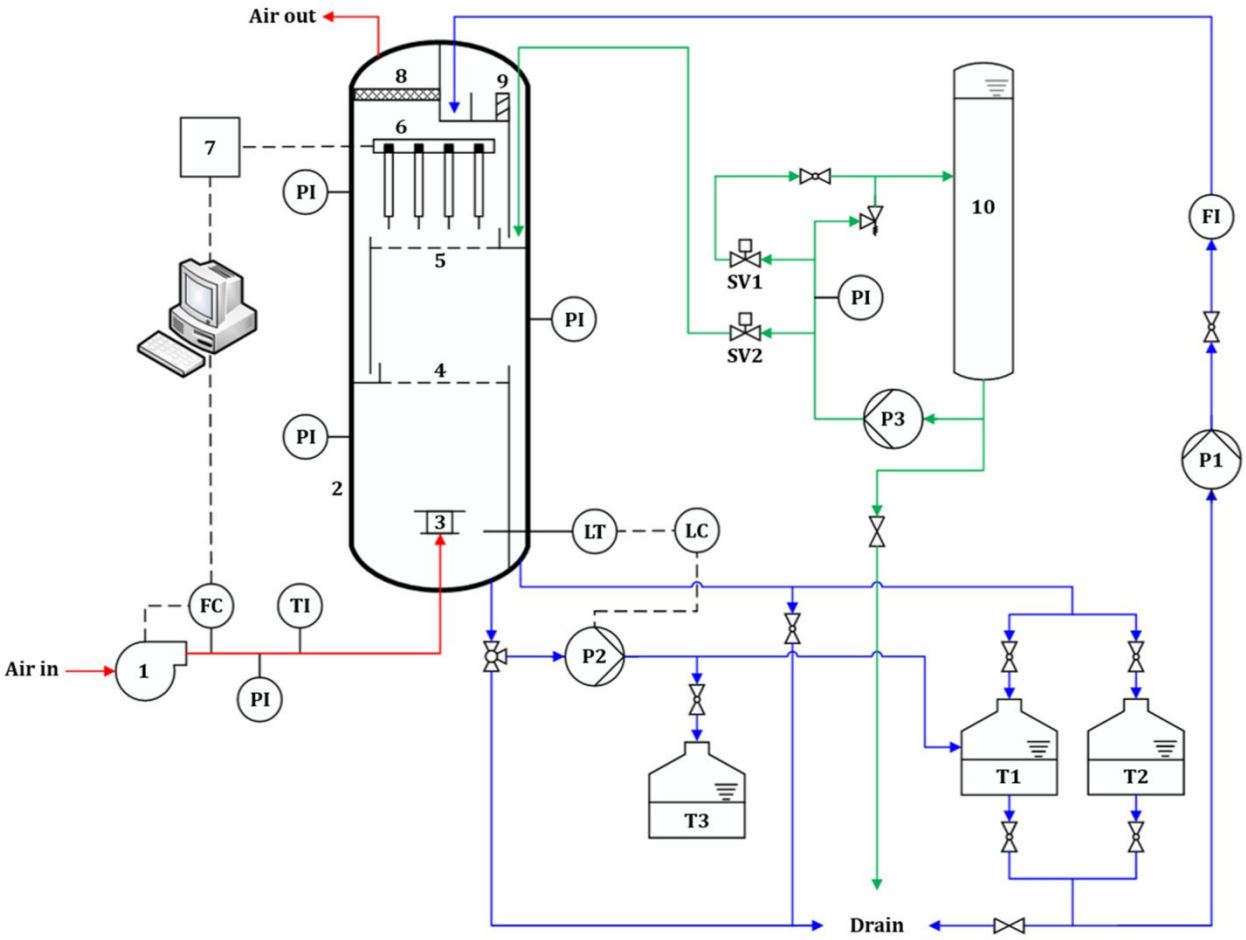

Figure 1. Schematic diagram of the column mockup facility (1 – air blower, 2 – tray column, 3 – air distributor, 4,5 – sieve trays, 6 – multiplex flow profiler, 7 – profiler electronics, 8 – demister pad, 9 – wire-mesh distributor, 10 – tracer batch column, FC – flow controller, FI – flow indicator, PI – pressure indicator, P1, P2, P3 – centrifugal pumps, SV1, SV2 – solenoid valves, TI – temperature indicator, T1,T2, T3 – tap water tanks, red lines – air, blue lines – tap water, green lines – deionized water (tracer), and dashed lines – signal line).

Table 1. Specifications of the experimental tray column.

Particulars	Dimensions
Internal column diameter	800 mm
Inlet weir (L × W × H)	532 mm × 2 mm × 35 mm
Outlet weir (L × W × H)	465 mm × 2 mm × 20 mm
Flow path length	620 mm
Active tray area	0.44 m^2
Hole specifications	3052 × 5 mm Ø, pitch: Δ × 12 mm
Fractional free area	13.55%
Downcomer clearance	20 mm
Tray spacing	365 mm
Tray thickness	15 mm
Calming zone	36 mm (inlet), 30 mm (outlet)

Air and tap water were used as working fluids. An adjustable high-pressure blower introduces the pressurized air at the bottom segment via a static baffle distributor (see Fig. 1). The distributor disperses the incoming air over the column cross-section uniformly. The pump P1 supplies the tap water from two separate 1 m^3 tanks (i.e., T1 and T2 in Fig. 1) to the top segment. The supply can be regulated via ball valve and rotameter. Upon interacting with the upflowing air on trays, the water gets recycled back to T1 and T2 hydrostatically. The wept liquid (collected in the bottom segment) can be transported to another tank (i.e., T3 in Fig. 1) for weeping measurements. Because of the intermittent actuation of the pump P2 by the two-level controller (see Fig. 1), the volume of liquid transported to T3 was monitored over multiple pump cycles to measure the average weeping rate. Additionally, a U-tube manometer measures the pressure exerted by liquid on the tray floor (i.e., 5 in Fig. 1). The time-averaged manometric head requires the gas momentum and capillary rise corrections (as suggested by Bennett et al.[40]) for calculating the clear liquid height. The gas loadings in the column in terms of *F*-factor were 1.77 $Pa^{0.5}$ and 2.05 $Pa^{0.5}$, whereas the weir loadings (w_L) were 2.15 $m^3m^{-1}h^{-1}$, 4.30 $m^3m^{-1}h^{-1}$ and 6.45 $m^3m^{-1}h^{-1}$. For these loadings, the corresponding weeping rates

(by sampling the liquid volume in T3 for 10 pump cycles) and clear liquid heights (by averaging the manometric heads measured at 10 regular intervals) on the tray are reported in Table 2.

Table 2. Liquid weeping and clear liquid height on the tray.

F-factor ($Pa^{0.5}$)	Weir loading ($m^3m^{-1}h^{-1}$)	Clear liquid height (mm)	Weeping rate (l/h)
1.77	2.15	7.76	148.36
	4.30	9.49	244.46
	6.45	10.35	474.28
2.05	2.15	8.40	20.73
	4.30	9.92	41.75
	6.45	10.92	89.60

A non-reactive and miscible tracer is essential for tracking the liquid flow and mixing patterns on the tray. Deionized water acts as an ideal tracer because of its low electrical conductivity and nearly identical physical properties as those of tap water. Initially, the pump P3 circulates the tracer back to the batch column (10) via solenoid valve SV1, while the other valve SV2 remains closed (see Fig. 1). Actuating SV2, automatically deactivates SV1 for a prescribed duration, which allows delivering a certain tracer volume immediately behind the inlet weir via 16 identical sub-pipes in a binary tree arrangement. Successive trials confirmed a total tracer discharge of 1.38 l/s, approximately, for different actuation times of SV2.

2.2 Multiplex flow profiler

Fig. 2a depicts the multiplex flow profiler mounted above the sieve tray (refer to Fig. 1) for determining the distributions of effective froth height, liquid holdup, and residence time. The profiler consists of a skeletal grid of 28 × 32 headers that holds 776 dual-tip conductivity probes. Each probe is connected to the profiler electronics via header grid as exemplarily shown for a 4 × 4 grid in the

electronic scheme in Fig. 2b. These probes uniformly span over the active tray area with a spatial resolution of 21 mm × 24 mm based on the inter-probe distance.

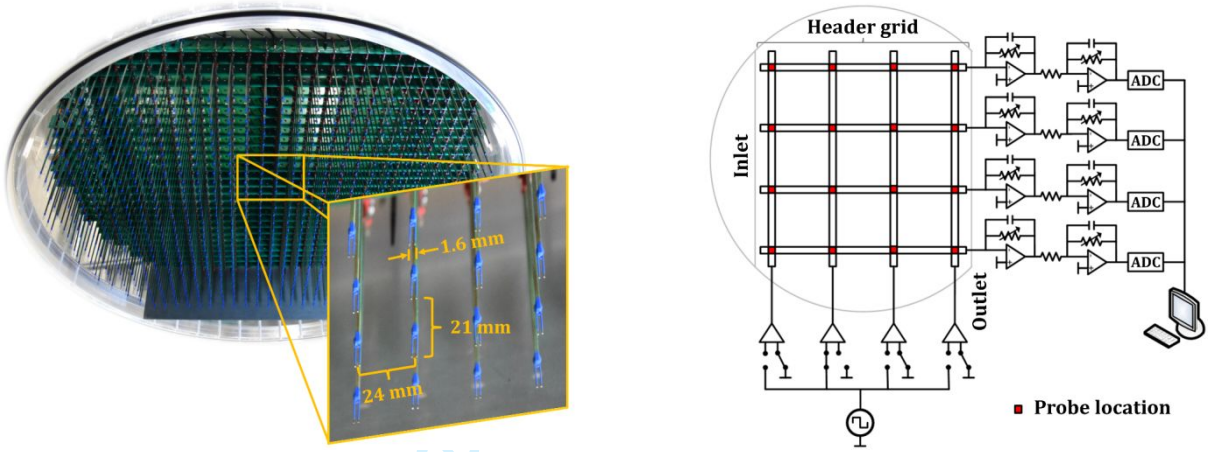

(a) (b)

Figure 2. (a) Multiplex flow profiler with probe details, and (b) electronic scheme exemplarily shown for a 4 x 4 arrangement.

Each probe is basically a multi-layer printed circuit board housing three separate electrodes namely transmitter, receiver and shielding in an insulating sheath enclosure (not specifically shown here). Only the tips of transmitter and receiver electrodes are to be exposed to the two-phase dispersion above the tray. As illustrated in Fig. 2b, an excitation voltage (i.e., DC bipolar) is applied to each header (parallel to the weir) sequentially via multiplexing scheme, which activates the corresponding transmitter electrodes. Parallel sampling of all longitudinal headers returns signals from all probe receivers based on the local instantaneous conductance near the probe tips. The acquired signals were appropriately amplified, digitized and structured into a 3D data matrix of size 32 × 28 × n for post-processing. Here, n is the product of the total measurement time and the sampling frequency (= 5000 Hz). Based on this procedure, the two-phase planar data were gathered by the profiler at multiple elevations above the tray deck via vertical adjustments. Further details of the multiplex flow profiler can be found elsewhere.[36,37]

3. Methodologies for hydrodynamic characterization

In industrial columns, the trays are often operated in the froth regime.[3,41] According to Bennett et al.,[40,42] the two-phase froth on a tray deck mainly consists of a liquid-continuous region that encloses irregular gas jets and bubbles. Above this region, a gas-continuous layer with liquid droplets (created by bubble rupturing) exists as shown in Fig. 3. As dispersion characteristics of these regions differ from each other, their hydrodynamic and mass-transfer behavior demand individual considerations.[43] In this work, the hydrodynamic behavior of the liquid-continuous region (i.e., bounded by effective froth height (h_{EF}) and tray deck, respectively, in Fig. 3) is studied, because the majority of the liquid is contained in that region.[42] Thus, the first step is to locate h_{EF} for identifying the uppermost boundary of the liquid-continuous region. Within this region, the experiments must be performed for determining the liquid holdup and tracer-based flow patterns as discussed below.

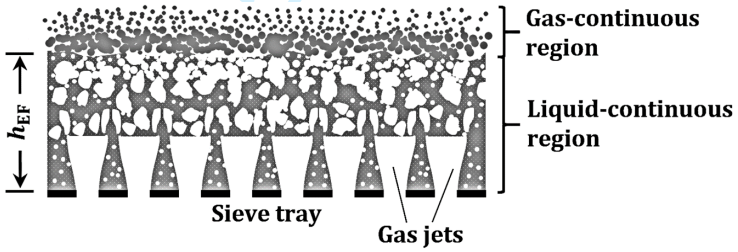

Figure 3. Froth shown over the sieve tray.

3.1 Effective froth height determination

The froth height estimation by Lockett et al.[41] is the only known approach available in the literature. In their study, the visually-estimated heights corresponded to the local liquid holdup of 10% in the γ-ray densitometry-led vertical liquid holdup profiles measured in a rectangular tray column. A verification of this criterion for froth height measurements is still pending (even for the circular columns), whereas the froth height distribution over the entire tray area is unavailable elsewhere. In

this regard, the only exception is the recent work of Vishwakarma et al.[39] proposing a new approach based on the data gathered by the multi-probe flow profiler described above. That approach analyzes the response of each probe exposed to the single-phase and two-phase flows of air and water. The probe response is mainly governed by the local fluid dynamics and the so-called geometry factor of the tips. At first, the two-phase dispersion data were acquired by the probes between 20 mm and 100 mm elevations above the tray in 10 mm increments. The duration of data recording at each elevation was 300 s. Such data are exemplarily shown for the probe [17,17] at 20 mm, 40 mm and 60 mm elevations in Fig. 4a for the loadings 2.15 $m^3m^{-1}h^{-1}$ and 2.05 $Pa^{0.5}$. In this figure, the probe exposure to gas only (i.e., L_0) is shown by the zero signal. When the probe tips are immersed in a liquid pool, the majority of the current from the transmitter tip goes to the associated receiver tip (because of the high geometry factor), whereas the remaining current dissipates to the nearby probes at ground potential (refer to the electronic scheme in Fig. 2b). The resulting probe response is represented by L_1 in Fig. 4a for the same temperature and conductivity of liquid in the pool as those in the two-phase experiments. In the case of a liquid droplet covering the probe tips, no current can dissipate to the nearby probes, and hence, the corresponding probe signal is higher than L_1 (not shown here). Based on these responses, the simplified probe signals corresponding to the two-phase dispersion are depicted in Fig. 4b.

In the liquid-continuous region, the dispersed gas surrounding a probe limits the current dissipation to the nearby probes, which returns the digital values higher than L_1. When a larger gas volume approaches the probe tips, the surface tension of the liquid initially hinders the gas penetration for a short duration. This reduces the geometry factor of the tips for that duration causing probe responses below L_1 (i.e., with negative slope). Then, zero values (= L_0) are registered for the gas volume enveloping the probe tips until the continuous liquid with dispersed gas appears again in the probe vicinity. These events and the corresponding probe responses are shown sequentially in Fig. 4b.

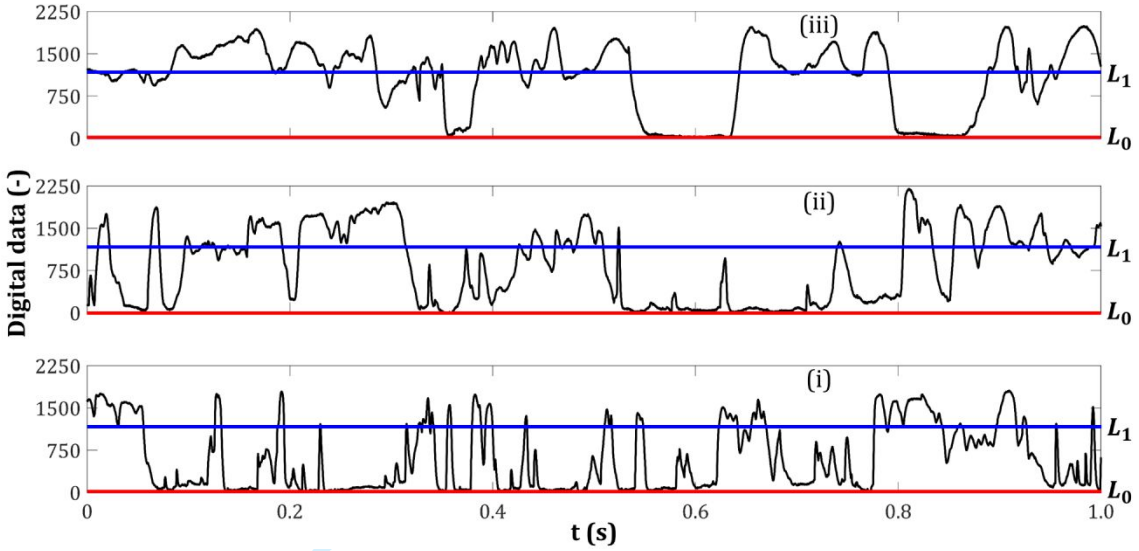

(a)

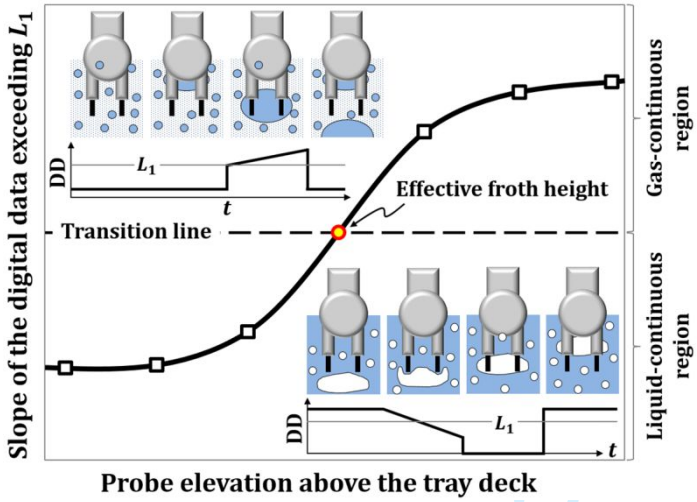

(b)

Figure 4. (a) Digital data of the probe [17,17] at (i) 20 mm, (ii) 40 mm and (iii) 60 mm elevations above the deck for 1 s duration (with L_0 and L_1 representing the gas-only and the liquid-only signals, respectively), and (b) simplified depiction of the probe response to the two-phase dispersion and froth height estimation based on the overall slope of the digital data exceeding L_1 (DD represents digital data in Fig. 4b, same notion holds for Figs. 5 and 6).

In the gas-continuous region with dispersed liquid droplets, a probe initially records the digital values marginally higher than L_0. The liquid droplets tend to settle over the probe shaft and gravitate, while coalescing below the lower end of that shaft. Then, the coalesced droplet slides down to the probe

tips and permits the current flow between them. The descending droplet also causes a steady increase in the geometry factor of the tips resulting in the digital values higher than L_1 (i.e., with positive slope). As the droplets falls down from the probe, the probe response resets to the values marginally higher than L_0. These occurrences and the respective probe responses are also presented sequentially in Fig. 4b.

Fig. 4b illustrates that the overall slope of the digital data above L_1 is negative for the liquid-continuous region and positive for the gas-continuous region. Therefore, each instance of the probe signal exceeding L_1 was retrieved and arranged on a dimensionless time-scale for the given elevations (not shown here). When fitted with a straight line, the arranged data exhibited a negative slope in the liquid-continuous region and a positive slope in the gas-continuous region. A trend of the calculated slopes is exemplarily shown in Fig. 4b, which is nearly linear between the data points immediately above and below the horizontal transition line (i.e., with zero slope). A linear interpolation between those data points provides the local effective froth height (h_{EF}) for that probe. This approach was applied for each probe resulting in the effective froth height distribution over the active tray area.

3.2 Liquid holdup calculation

Fig. 5 highlights the algorithm used for determining the local liquid holdup corresponding to each probe above the tray deck. Each step involved in this algorithm is summarized below sequentially:

- **Data acquisition:** The two-phase dispersion data were recorded between 20 mm and 100 mm elevations above the deck in 10 mm increments. The duration of data recording at each elevation was 300 s (already shown in Fig. 4a for a limited time scale).
- **Phase referencing:** Phase referencing refers to obtaining the characteristic response of a probe to the gas-only and the liquid-only exposure. The respective digital values are referred to as L_0 and L_1 in Figs. 4a and 5.

- **Threshold determination:** The most common and robust phase discrimination technique is the single threshold method.[44,45] A threshold is a certain fraction of the difference between L_1 and L_0 as illustrated in Fig. 5. Based on a separately-available measurement campaign[36] involving the applications of γ-ray computed tomography and a prototype 3 × 3 profiler, the value of the threshold T was selected as $0.75L_1$ for each probe.
- **Signal binarization:** Using the threshold T, the digital data (corresponding to the two-phase dispersion) for the given elevations were binarized into time instances of the probe exposure to liquid and gas (see the example shown in Fig. 5).
- **Holdup calculation:** The time instances of the liquid occurrence in the binary signal were summed up. The ratio of that sum and the total measurement time is the time-averaged local liquid holdup. Repeating the overall procedure for each probe at each elevation resulted in the 3D liquid holdup distribution.

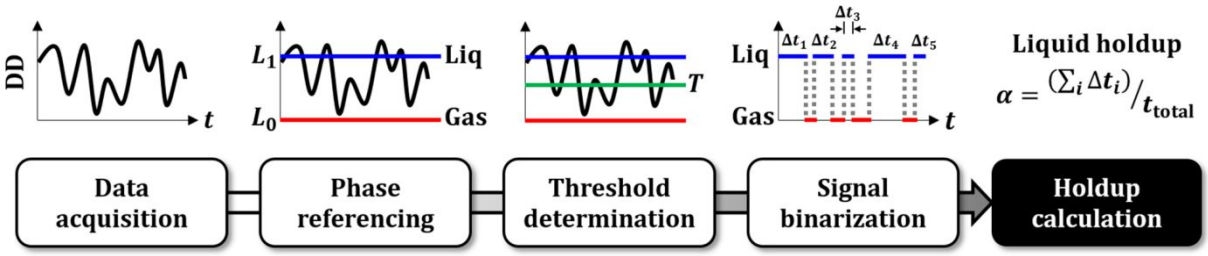

Figure 5. Schematics of the algorithm for calculating local liquid holdup.

According to Vishwakarma et al.,[36] this algorithm cannot distinguish whether the holdup data belongs to the liquid- or gas-continuous region. Therefore, the holdup values above the local effective froth height (h_{EF}) for each probe were ignored for obtaining the holdup variation along the froth height for the prescribed loadings.

3.3 Tracer-based flow monitoring

Fig. 6 presents the sequence of steps involved in the tracer-based flow monitoring on the tray. These steps are summarized below sequentially:

- **Reference data acquisition:** Acquiring the two-phase dispersion data, while maintaining uniform liquid conductivity (κ) was the first step (similar to Fig. 4a). This was performed by applying deionized water, tap water and their mixture, serially, to cover the liquid conductivity range expected during the tracer measurements later (see Fig. 6). The total duration of data sampling was 60 s.
- **Data filtering and smoothing:** The filtering and smoothing schemes (referred to as 'intermittent window averaging' and 'moving average smoothing', respectively) were employed for extracting the liquid flow information from the two-phase dispersion data. An elaborate description of these schemes are available elsewhere.[36]
- **Digital data – conductivity relationship:** A linear relationship between the extracted liquid data and the liquid conductivity was obtained for the given conductivity range (see Fig. 6). A unique relationship was determined for every probe as well as for each combination of gas and liquid loadings.

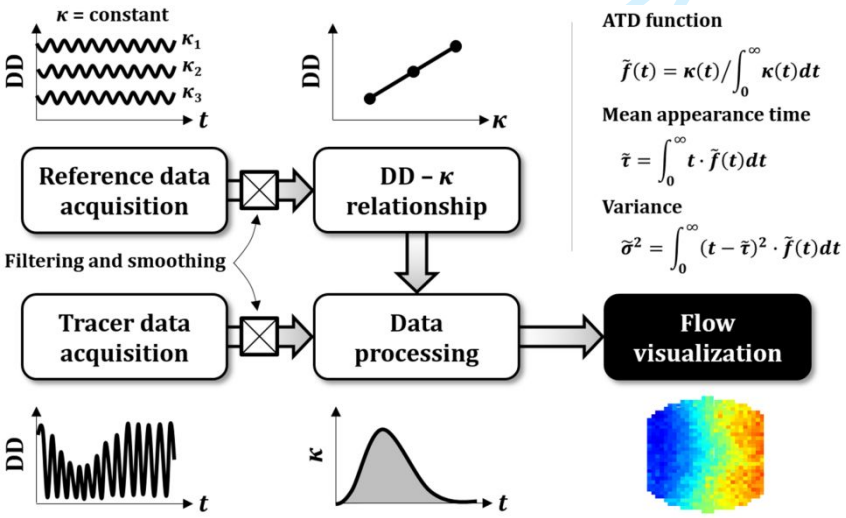

Figure 6. Sequence of operations for the tracer-based flow monitoring.

- **Tracer data acquisition:** The recording of the two-phase dispersion data was initiated immediately after the tracer pulse input (refer to Section 2.1). The duration of the tracer injection was 2 s, whereas the sampling duration remained unchanged. An exemplary probe response after tracer injection is shown in Fig. 6. Eventually, the tracer flow information from the dispersion data was retrieved through application of the **filtering and smoothing schemes** mentioned earlier.
- **Data processing:** Based on the linear relationship between the extracted data and the liquid conductivity, the time-dependent liquid conductivity profile was obtained for each probe. Further processing involved curve fitting (i.e., based on the solution of the axial-dispersion model) followed by flipping and orienting the fitted function (see Fig. 6 for the resulting function). These operations are thoroughly illustrated in another study.[36]
- **Flow visualization:** The tracer-tagged liquid flow over the deck was visualized via time distribution of the tracer appearance at the probe tips. According to Walton,[46] a linear relationship exists between the tracer concentration (i.e., equal to the total quantity of inherent dissolved salts in the liquid) and the liquid conductivity for the observed conductivity range. Thus, the appearance time distribution (ATD) function, i.e., $\tilde{f}(t)$, and its parameters (mean appearance time ($\tilde{\tau}$) and variance ($\tilde{\sigma}^2$)) were obtained for each probe using the corresponding conductivity profile as shown in Fig. 6. The distribution of mean appearance time ($\tilde{\tau}$) informs the tracer flow patterns, whereas the variance ($\tilde{\sigma}^2$) distribution reveals the mixing profiles of tracer on the tray (similarly followed by Bell[26,47] and Solari and Bell[29]). Dividing the longitudinal distance between any two probes along a row by the difference in their respective mean appearance times provides the local unidirectional liquid velocity.[29] Then, the RTD function and the corresponding parameters (similar to those given in Fig. 6) were obtained for the entire tray via probe-wise averaging of the time-dependent tracer data at the tray boundaries.

4. Hydrodynamic description of the operational sieve tray

4.1 Effective froth height distribution

Fig. 7 depicts the froth height distributions along with the average values for the prescribed loadings. A systematic rise in the average froth height with increasing weir loading is observed for each gas loading. It is related to the increase in the liquid inventory (over the deck) with the weir loading at a constant *F*-factor. This trend is likely to continue beyond the studied loadings until the liquid weeping from the tray becomes severe (see Table 2 for reference). Severe weeping would restrict any further growth in the liquid inventory resulting in the constant average froth height thereafter. For each weir loading, higher *F*-factors lead to higher froth heights, and vice-versa (see Fig. 7). Here, the capability of the gas flow to suspend liquid chunks and droplets above the deck increases with the *F*-factor. These observations also hold for the local effective froth heights for the given loadings in Fig. 7, which is further shown by the local effective froth heights along transverse and centerline axes on the tray in Fig. 8. Figs. 7 and 8 confirm a reasonable homogeneity in the effective froth height over the deck, except in the first quarter of the flow path length from the tray inlet. The lowest froth heights are observed immediately after the inlet weir, because of the low aeration above the inlet calming zone (see Fig. 8a). Afterwards, the incoming liquid flow (i.e., directed by wall curvature and downcomer backup) interacts with the upflowing gas. The cross-flow interaction between the two phases along the flow path length imparts momentum and trajectory to the flowing froth, which results in the sudden increase of the effective froth height up to the maximum (refer to Fig. 8a). A gradual decrease in the effective froth height follows thereafter, that is caused by the steady reduction of the froth momentum until the height becomes nearly uniform. These observations can also be visualized in the velocity vector maps later in Section 4.3. Górak and Olujić[2] also reported the existence of froth height

gradients on large trays, with the highest froth prevailing near the tray inlet due to the considerable flow resistance encountered by the liquid from gas jets and bubbles there. The respective locations of minimum and maximum froth height in Fig. 8a remain consistent throughout for the studied loadings.

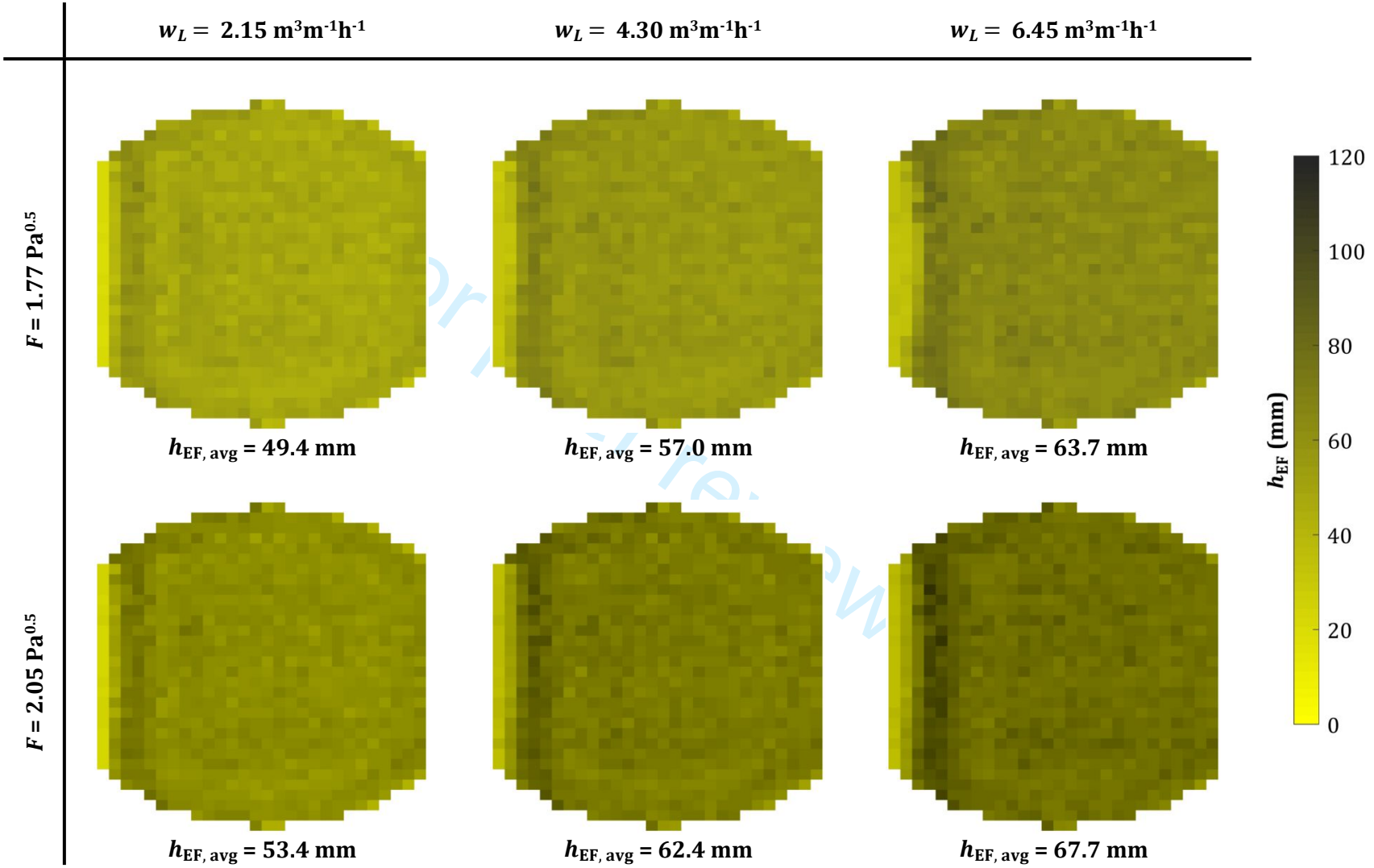

Figure 7. Effective froth height distribution for the prescribed loadings (left edge – tray inlet, right edge – tray outlet, same notion holds for all other parameter distribution data below).

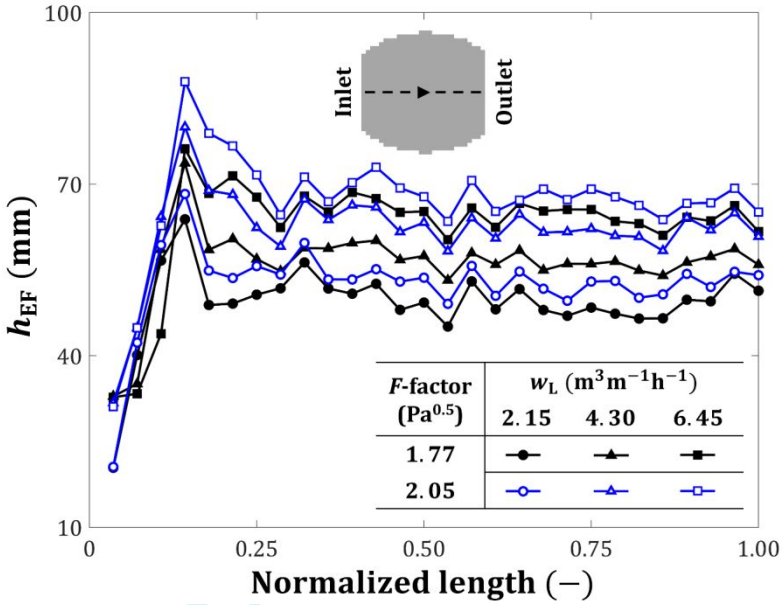

(a)

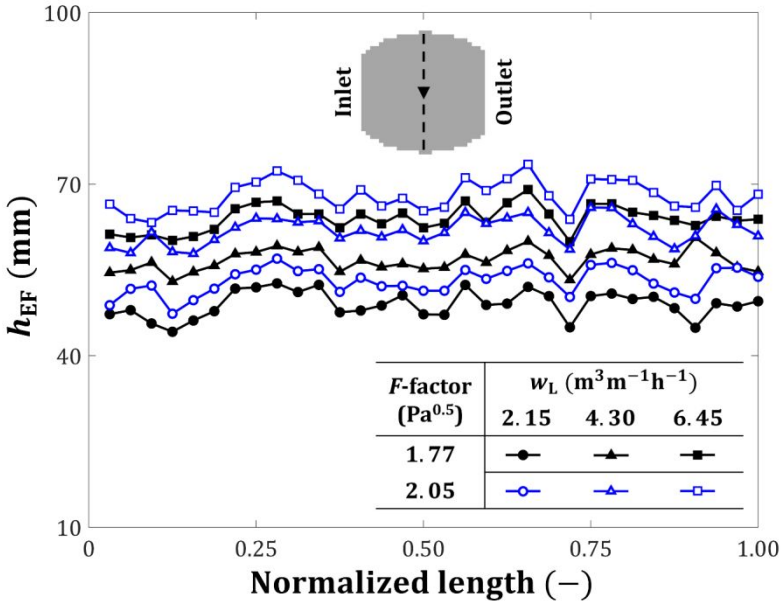

(b)

Figure 8. Effective froth height distribution along (a) the transverse axis and (b) the tray centerline.

Thus, a similar two-phase flow behavior is expected for these loadings in the holdup measurements. Further processing of the digital data (in Section S1.1 in the Supplementary Information) confirms an excellent reproducibility of the average effective froth heights mentioned in Fig. 7. Besides, the

criterion proposed by Lockett et al.[41] for froth height estimation (see Section 3.1) is evaluated in the next section considering the available holdup data there.

4.2 Liquid holdup distribution

Fig. 9 shows the liquid holdup distribution at each profiler elevation (up to 70 mm) for the studied loadings. The intentionally black-dyed pixels in this figure mask the holdup data for the probes, whose elevation exceed their respective h_{EF} (displayed in Fig. 7). In other words, the holdup values beyond the local effective froth height are omitted. Such masking permits obtaining a realistic holdup distribution at each measuring plane above the tray deck. Consequently, the average liquid holdup at each profiler elevation (by replacing masked pixels with the zero values) are presented in Figs. 9 and 10 for these loadings.

In Fig. 9, higher liquid content immediately after the inlet weir is followed by a sudden decrease along the flow path at 20 mm and 30 mm elevations. The higher liquid holdup is also attributed to the very low aeration of the liquid above the inlet calming zone, which coincides with the minimum froth height (see Figs. 7 and 8). Immediately after the calming zone, however, the momentum of the entering liquid (because of the downcomer backup) is sufficient to resist the upflowing gas, thereby sustaining higher liquid holdups. The liquid holdup in these regions from 30 mm onwards (wherever applicable) is governed by weir loading, liquid weeping (especially at lower gas load) and minor aeration (because of the splashed liquid falling backwards from the leading flow path). After these regions along the flow path, the interaction of the upflowing gas and the longitudinally-flowing liquid near 20 mm elevation imparts momentum and trajectory to the flowing froth (as discussed in Section 4.1) resulting in the higher aeration there. In this region, the liquid holdup tends to increase with profiler elevation until the froth approaches the maximum effective height (compare Figs. 7 and 9).

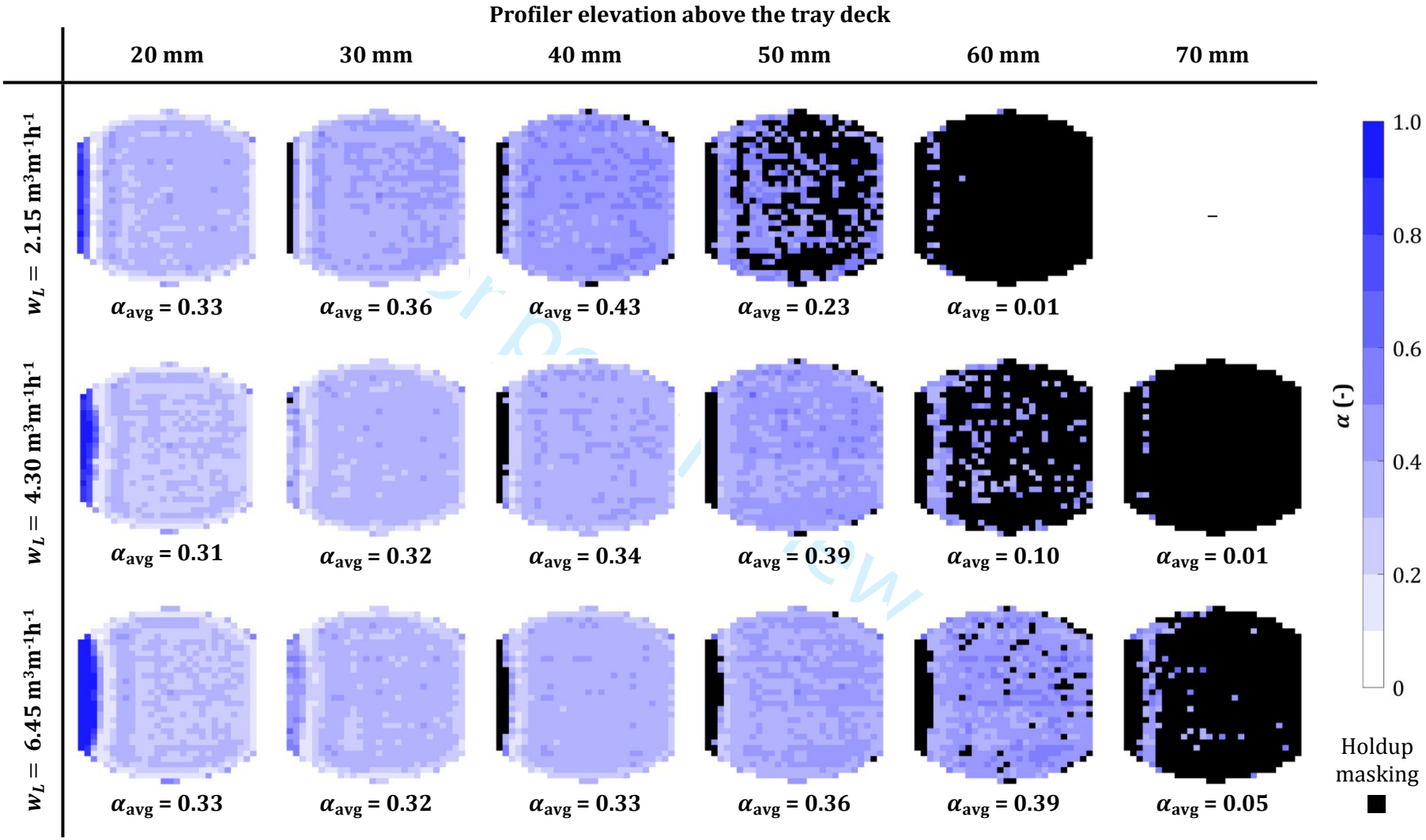

(a) *F*-factor = 1.77 $Pa^{0.5}$

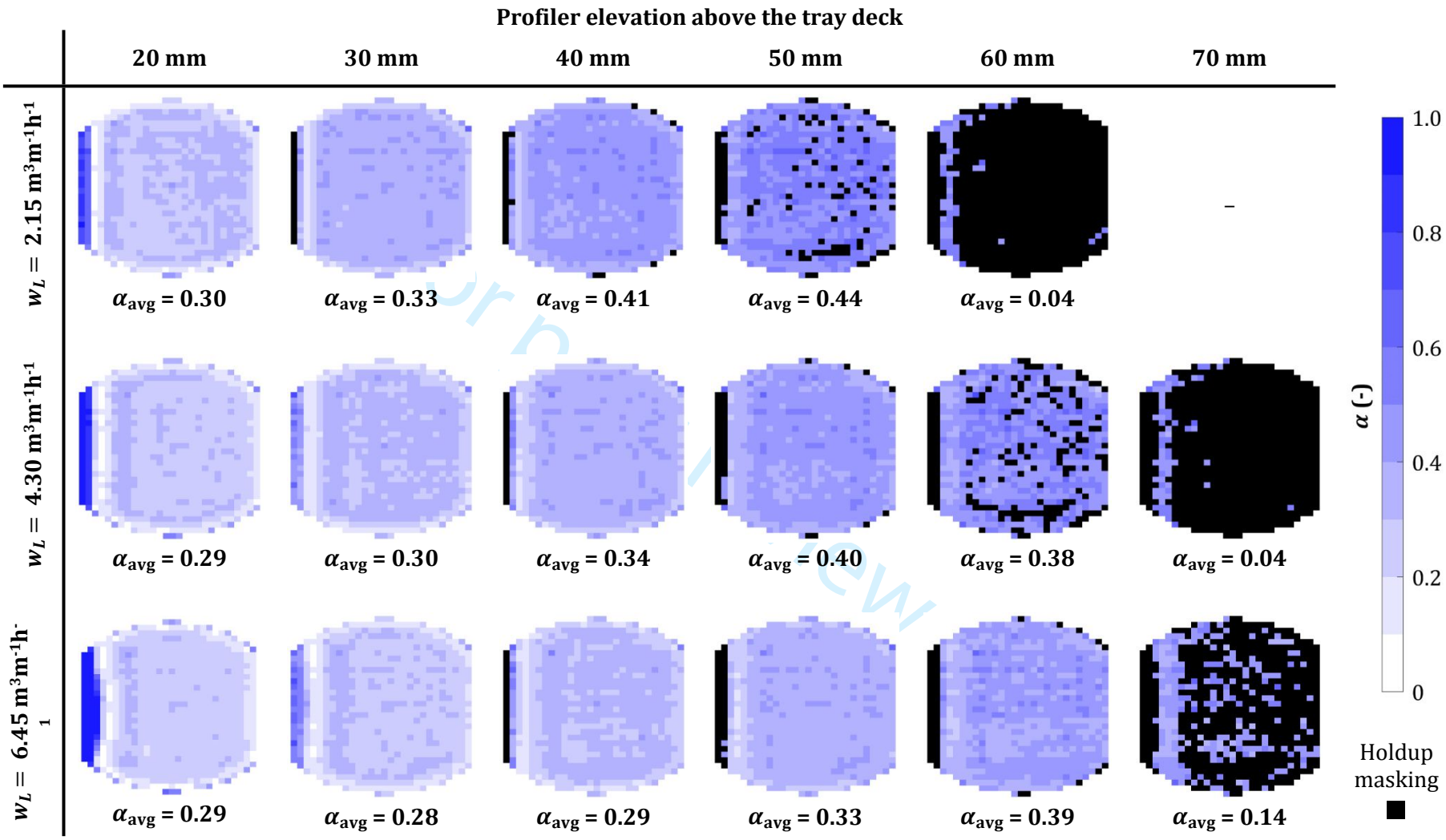

(b) F-factor = 2.05 $Pa^{0.5}$

Figure 9. Liquid holdup distribution above the tray deck for the prescribed loadings (black pixels – masked holdup values for the probes, whose elevation exceed their respective h_{EF} values).

Further along the flow path, the froth momentum and height reduce upon achieving the maximum elevation and become steady thereafter leading to approximately uniform liquid holdup distribution over the remaining tray deck (see Figs. 7 to 9). In that area, a rise in the liquid holdup with profiler elevation is observed because of the liquid suspension by gas jets from the lower elevation (see the video provided in the Supplementary Information). Besides, the homogeneity in the liquid holdup distribution over the referred area largely persists for the given elevations until the profiler approaches the average effective froth height. Near this elevation, the holdup distributions are comparatively non-uniform, because of the random rise and fall of suspended liquid combined with chaotic liquid splashing.

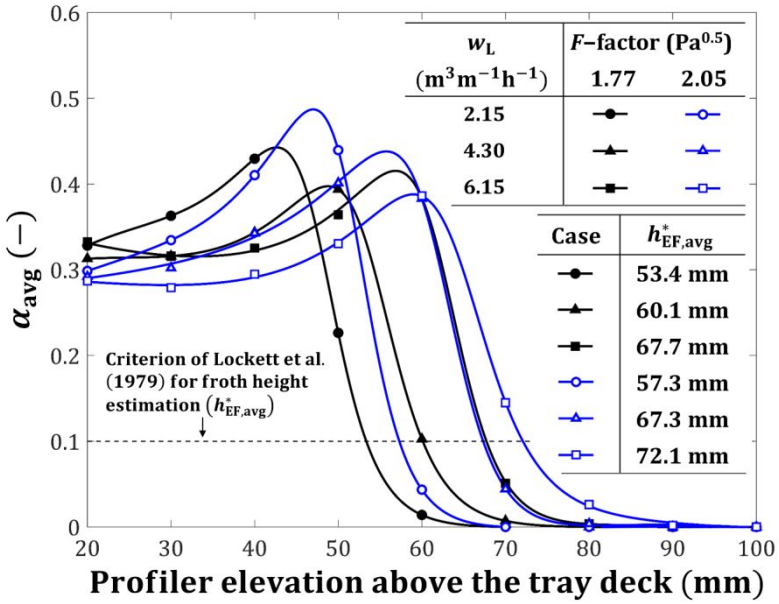

Figure 10. Average liquid holdup versus profiler elevation for the given loadings.

The overall liquid holdup at different profiler elevations can be better analyzed using Fig. 10. The holdup data in this figure are fitted with cubic/quartic rational functions (for visualization purpose only). Firstly, the gas jets emerging from the tray deck (see the video provided in the Supplementary Information) project the surrounding liquid to higher elevations causing a lower liquid holdup at

lower profiler elevations. The gas jets tend to break at certain height, and hence, a comparative increase in the liquid holdup with the profiler elevation is observed in Fig. 10. As the majority of the suspended liquid achieves the maximum elevation close to the average effective froth height, the highest liquid holdup appears there for the given loadings in Fig. 10. Further, the liquid holdup reduces drastically beyond the effective froth height because only a small portion of the liquid-continuous dispersion appears above that elevation (see Fig. 9, too). Further processing of the two-phase dispersion data (in Section S1.2 in the Supplementary Information) confirms an excellent reproducibility of the average liquid holdups provided in Figs. 9 and 10. Fig. 10 also shows the criterion of Lockett et al.[41] that is represented by a horizontal line corresponding to the 10% average liquid holdup. The intersection of this line with the holdup profiles (i.e., rational functions) predicts the average effective froth height (referred to as $h^*_{\mathrm{EF,avg}}$) for the studied loadings. This criterion slightly overestimates $h_{\mathrm{EF,avg}}$ by 3 to 5 mm, whereas the maximum deviation in the values of $h^*_{\mathrm{EF,avg}}$ with respect to those of $h_{\mathrm{EF,avg}}$ is 8.1% (compare Figs. 7 and 10). Overall, the referred criterion estimates the average effective froth height with sufficient accuracy in the circular column, too.

4.3 Liquid flow and mixing patterns

Since the tracer-response analysis is extensive in terms of experimentation and data post-processing, the two-phase flow behavior at 40 mm elevation was considered as a representative of the froth regime for each tray loading.[36] This elevation below the average effective froth height also ensures the probe exposure to the liquid-continuous region (except near the tray inlet as evident from the holdup masking in Fig. 9). Therefore, the data gathered by the first two probe columns immediately after the tray inlet were disregarded in the calculations. According to the procedure reported in Section 3.3, mean appearance time ($\tilde{\tau}$) and variance ($\tilde{\sigma}^2$) were computed for each probe. From three experimental runs, the average of $\tilde{\tau}$ and $\tilde{\sigma}^2$ were calculated for each probe, and the corresponding distributions are shown in Fig. 11 and 12, respectively. The processed experimental data show an

adequate reproducibility (see Section S1.3 in the Supplementary Information). For better visualization, the isocontours are provided in Figs. 11 and 12 via averaging of the pixel data using those of the surrounding pixels. The unidirectional liquid velocities for the studied loadings are also illustrated in Fig. 13, where the arrow lengths represent the velocity magnitudes. The liquid velocities are shown at five equidistant planes parallel to the weir using the mean appearance time distributions presented in Fig. 11.

Figs. 11 to 13 exhibit a reasonable symmetry in the flow and mixing characteristics of the liquid phase with respect to the tray centerline. Similar observation has been reported by several earlier experimental studies mentioned in Section 1. The liquid backup in the downcomer is pushed towards the tray centerline by the wall curvature causing a parabolic velocity distribution (with peak velocities along the centerline) over a certain tray area after the inlet (see Fig. 13).[26] Consequently, lower mean appearance times and variances appear in Figs. 11 and 12 over the tray area with higher liquid velocities in the parabolic distribution. Further along the flow path length, the velocities over the majority of the tray deck homogenize as a result of the gas flow resistance and agitation (refer to Fig. 13). Consequently, a systematic rise in mean appearance time and variance can be seen in Figs. 11 and 12 over the majority of the tray bubbling area. Immediately before the tray outlet, however, a marginal increase in liquid velocity (see Fig. 13) owing to the contracting flow passage caused by the converging wall geometry is observed regardless of the gas and liquid loadings.

At constant *F*-factor, the liquid velocity at any tray location increases with the weir loading, and vice-versa (see Fig. 13). At the same time, mean appearance time and variance reduce (see Figs. 11 and 12). Similarly, at a fixed weir loading, the liquid velocity at any particular tray location is expected to increase with decreasing *F*-factor. This can happen because the overall resistance offered by the up flowing gas to the liquid flow drops with the *F*-factor. However, the opposite behavior is observed in Fig. 13, because of the higher liquid weeping at the lower *F*-factor (see Table 2). Eventually, higher

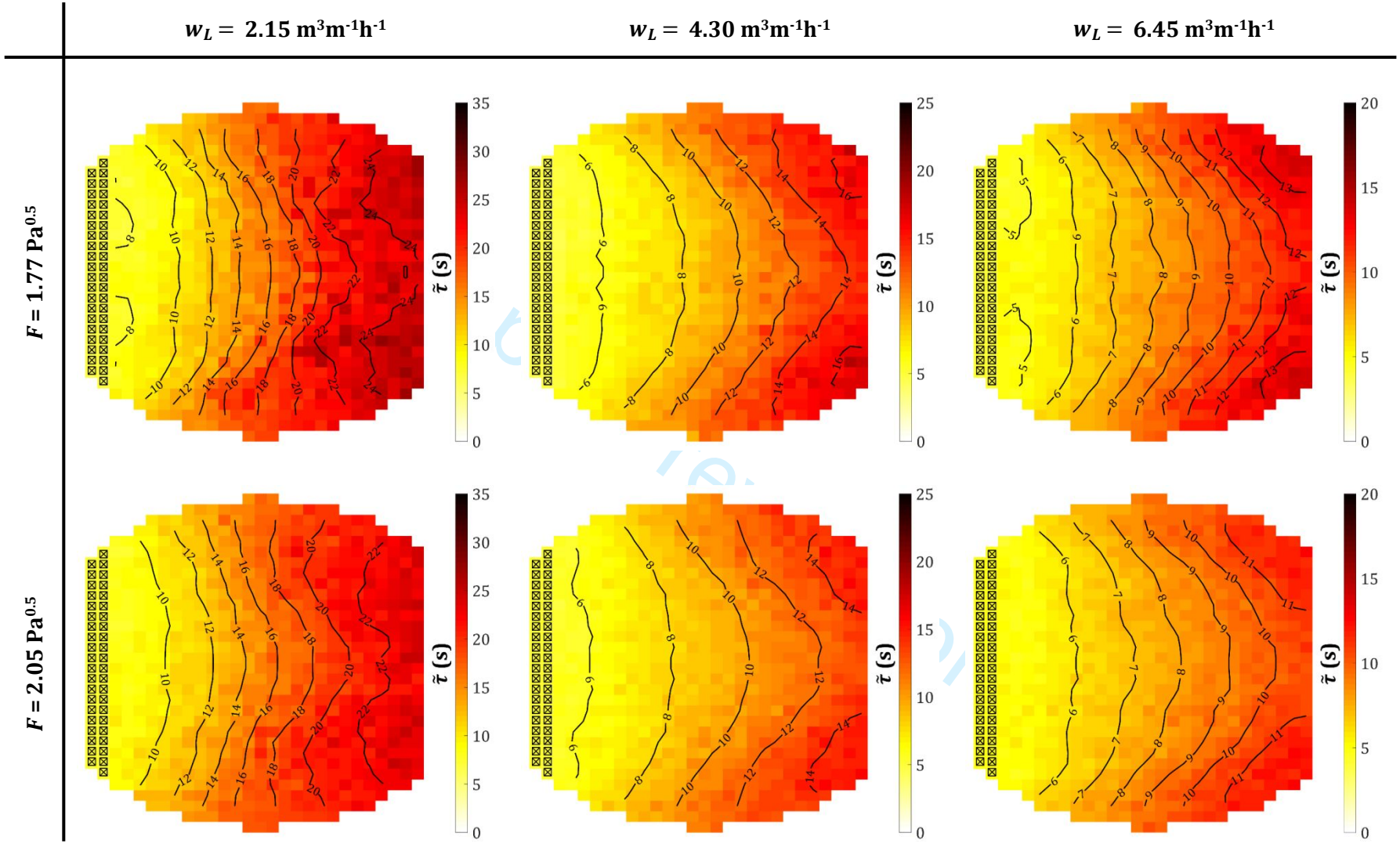

Figure 11. Mean appearance time distributions of tracer for the given loadings at 40 mm profiler elevation (crossed boxes: probe columns disregarded since they are located above the effective froth height, same notion holds for Figs. 12 and 13).

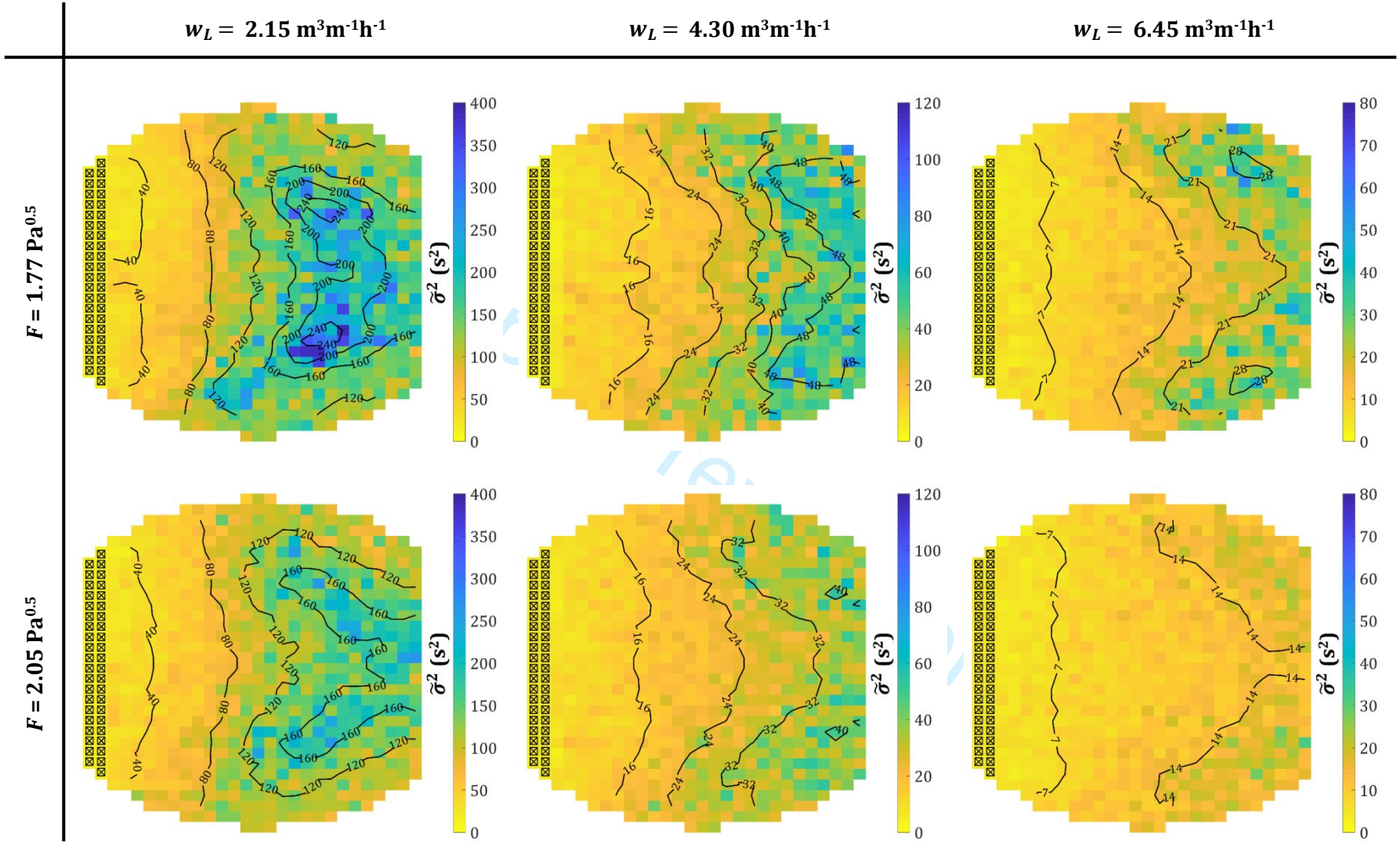

Figure 12. Variance distributions of tracer for the given loadings at 40 mm profiler elevation.

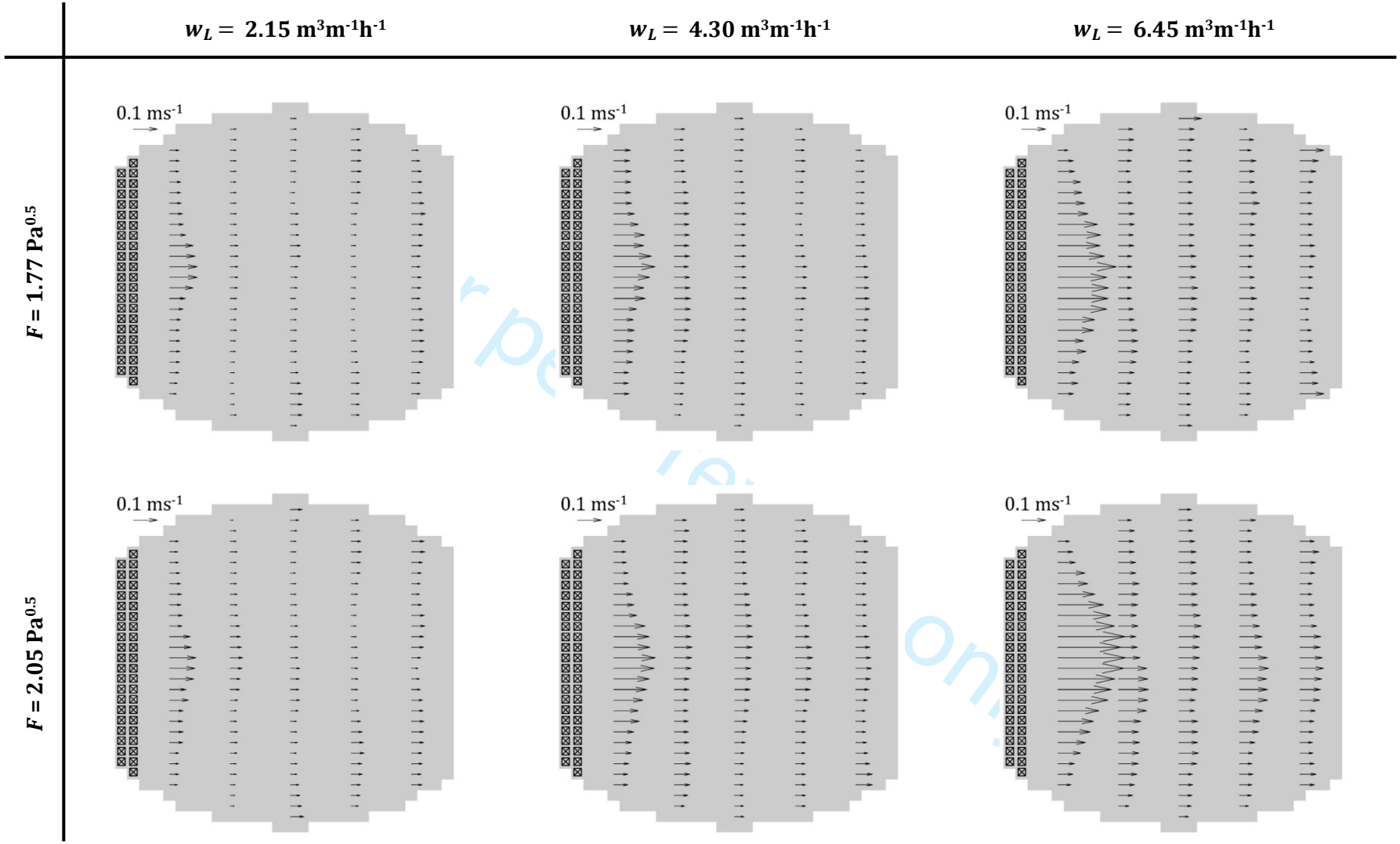

Figure 13. Maps of unidirectional velocity vectors for the given loadings at 40 mm profiler elevation.

mean appearance times and variances are observed at the lower *F*-factor for the given weir loadings (see Figs. 11 and 12).

The overall liquid flow characteristics in the two-phase dispersion above the deck were determined via residence time distribution (RTD). As the first two probe columns (parallel to the weir) are ignored in Figs. 11 to 13, the conductivity data corresponding to the probes on the third column (now referred to as 'profiler inlet') and the last column (now referred to as 'profiler outlet') were averaged using the liquid holdup and mean appearance time data as

$$\overline{\kappa}(t) = \frac{\sum_{i=1}^{j} \frac{\kappa_i(t) \cdot \alpha_i}{\tilde{\tau}_i}}{\sum_{i=1}^{j} \frac{\alpha_i}{\tilde{\tau}_i}} \quad . \tag{1}$$

In Eq. 1, i represents the probe index, whereas j is the total number of probes in the respective column (i.e., on profiler inlet and outlet, separately). The averaged conductivity profiles corresponding to profiler inlet and outlet are exemplarily shown for the highest weir loading and *F*-factor in Fig. 14a. For other loadings, these profiles are shown in Fig. S1 in the Supplementary Information. Using the flow model fitting approach employed by Vishwakarma et al.[11,48] for deconvolution calculation, the RTD function ($f(t)$) and corresponding parameters (i.e., mean residence time (τ) and variance (σ^2)) were obtained for the studied loadings as illustrated in Fig. 14b. The mean residence time and the variance of the RTD function are defined as

$$\tau = \int_0^\infty t f(t) dt \,, \tag{2}$$

$$\sigma^2 = \int_0^\infty (t-\tau)^2 f(t) dt \,, \quad . \tag{3}$$

respectively. The definitions of the ATD and the RTD function (and the corresponding variances) are the same (see Fig. 6 and Eqs. 2 and 3). However, the notion of ATD refers to the probe-wise tracer toring, where the local control volume corresponding to any probe is unknown.[36] On the other hand,

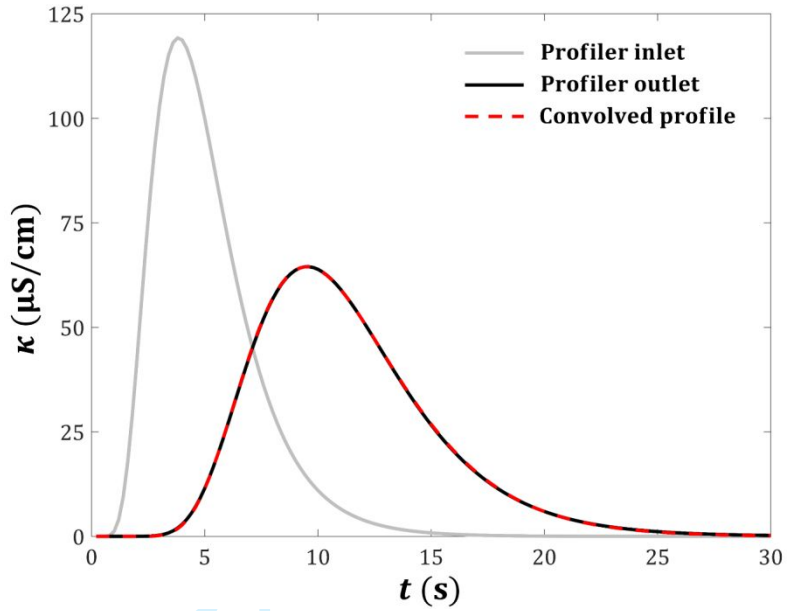

(a)

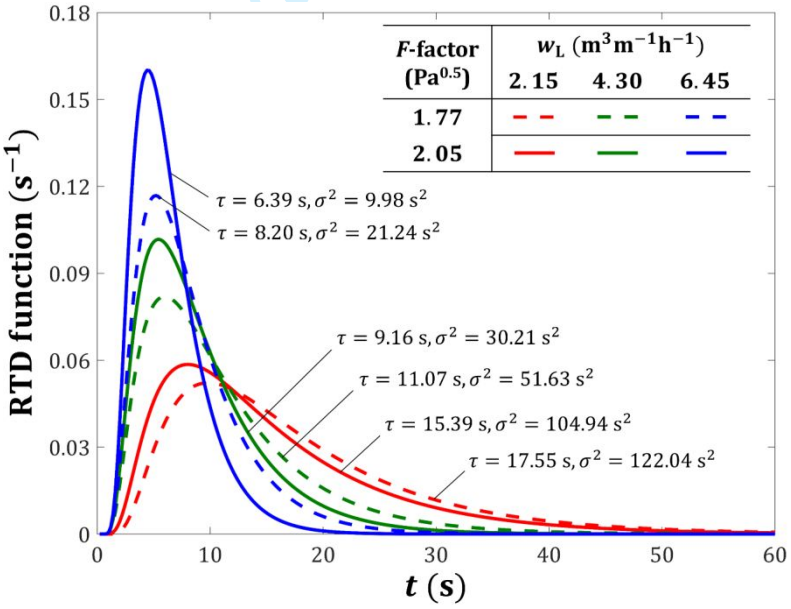

(b)

Figure 14. (a) Liquid conductivity profiles for 6.45 $m^3m^{-1}h^{-1}$ weir loading and 2.05 $Pa^{0.5}$ *F*-factor, and (b) RTD functions and associated parameters for the given loadings.

the notion of RTD refers to the tracer dispersion within the control volume (i.e., tray deck), whose boundaries are well-defined (i.e., profiler inlet and outlet here). Accordingly, mean residence time is the average time that the tracer spends between profiler inlet and outlet, whereas mean appearance

time is the average time taken by the tracer to appear at the probe tips immediately after the tracer injection. Furthermore, Fig. 14a also shows the convolved conductivity profile (i.e., equal to the convolution integral of the RTD function and the conductivity profile corresponding to profiler inlet) that exactly matches the conductivity data at the profiler outlet. This also applies to the other tray loadings (as shown in Section S2 in the Supplementary Information), which confirms the correct deconvolution calculation. In Fig. 14b, it is evident that mean residence time and variance reduce with increasing weir loading at constant *F*-factor. Secondly, for a fixed weir loading, mean residence time and variance increase with decreasing *F*-factor, because of the associated increase in liquid weeping (see Table 2). A physical explanation for these observations is already given in the previous paragraph, while referring to the distributions of mean appearance time, variance of the ATD function and liquid velocity in Figs. 11 to 13. It should be noted that the average of the mean appearance time data from three experimental runs were used in Fig. 11 and Eq. 1. For these runs, the best liquid conductivity data matching the average of the mean appearance time data were selected and used in Eq. 1. That selection was based on the lowest (absolute) average deviation of the mean appearance time data from one experimental run with respect to the data provided in Fig. 11. For the data illustrated in Fig. S1 in the Supplementary Information, the maximum deviation was 2.8% for the studied loadings.

5. Conclusion

An extensive characterization of the tray hydrodynamics in a large-scale tray column mockup has been performed using a conductivity-based multi-probe flow profiler. For the first time, 3D liquid holdup distribution, liquid RTD and effective froth height distribution have been reported for several gas and liquid loadings at high spatiotemporal resolution. The detailed flow and mixing patterns of the liquid in the two-phase dispersion have been retrieved via tracer-based experiments. The methodology for computing each of these distributions has been described in this work. A uniform

froth height was observed over the majority of the tray deck, whereas the minimum and maximum froth heights were detected immediately after the tray inlet. A homogenous liquid holdup distribution was also observed at multiple elevations above the deck with the highest holdups occurring near the average effective froth height. With respect to tray centerline, axisymmetric liquid flow and mixing patterns were detected with parabolic velocity distributions near the inlet. The liquid velocities over the remaining tray deck were nearly uniform for the studied loadings. Using experimental holdup and tracer data, the overall liquid mixing over the tray was quantified via residence time distribution. The reported data improve the benchmarking standards of the CFD models and permit a better validation of the tray efficiency prediction models.

Data availability

The processed experimental data reported in this work are provided in the RODARE repository.[49] The data corresponding to the distributions of effective froth height (Figs. 7 and 8), liquid holdup (Figs. 9 and 10), mean appearance time (Fig. 11), variance (Fig. 12) and liquid velocity (Fig. 13) are supplied with proper indexing in this repository. All these data are intended for non-commercial use only.

Funding

This work was supported by the German Academic Exchange Service (Deutscher Akademischer Austauschdienst, DAAD) [grant number 91563198].

Nomenclature

F	gas load F-factor ($Pa^{0.5}$)

$f(t)$	RTD function (s^{-1})
$\tilde{f}(t)$	ATD function (s^{-1})
h	height (mm)
t	time (s)
w_L	weir loading ($m^3m^{-1}h^{-1}$)

Greek Letters

α	time-averaged liquid holdup (-)
κ	liquid conductivity (μS/cm)
σ^2	second central moment of $f(t)$ (s^2)
$\tilde{\sigma}^2$	second central moment of $\tilde{f}(t)$ (s^2)
τ	mean residence time (s)
$\tilde{\tau}$	mean appearance time (s)

Abbreviations

ATD	appearance time distribution
RTD	residence time distribution

References

1. Zhao H, Li Q, Yu G, Dai C, Lei Z. Performance analysis and quantitative design of a flow-guiding sieve tray by computational fluid dynamics. *AlChE J.* 2019;65(5).

2. Górak A, Olujic Z. *Distillation: equipment and processes.* Academic Press; 2014.

3. Lockett MJ. *Distillation tray fundamentals.* Cambridge University Press; 1986.

4. Krishna R, Van Baten J, Ellenberger J, Higler A, Taylor R. CFD simulations of sieve tray hydrodynamics. *Chem Eng Res Des.* 1999;77(7):639-646.

5. Jiang S, Gao H, Sun J, Wang Y, Zhang L. Modeling fixed triangular valve tray hydraulics using computational fluid dynamics. *Chemical Engineering and Processing: Process Intensification.* 2012;52:74-84.

6. Li Q, Li L, Zhang M, Lei Z. Modeling flow-guided sieve tray hydraulics using computational fluid dynamics. *Industrial & Engineering Chemistry Research.* 2014;53(11):4480-4488.

7. Jiang B, Liu P, Zhang L, et al. Hydrodynamics and mass-transfer analysis of a distillation ripple tray by computational fluid dynamics simulation. *Industrial & Engineering Chemistry Research.* 2013;52(49):17618-17626.

8. Li X, Yang N, Sun Y, Zhang L, Li X, Jiang B. Computational fluid dynamics modeling of hydrodynamics of a new type of fixed valve tray. *Industrial & Engineering Chemistry Research.* 2014;53(1):379-389.

9. Malvin A, Chan A, Lau PL. CFD study of distillation sieve tray flow regimes using the droplet size distribution technique. *J Taiwan Inst Chem Eng.* 2014;45(4):1354-1368.

10. Vishwakarma V, Rigos N, Schubert M, Hampel U. Efficiency estimation of tray columns based on flow profiles and vapor–liquid equilibrium characteristics of binary mixtures. *Ind Eng Chem Res.* 2019;58(51):23347-23358.

11. Vishwakarma V, Schubert M, Hampel U. Assessment of separation efficiency modeling and visualization approaches pertaining to flow and mixing patterns on distillation trays. *Chem Eng Sci.* 2018;185:182-208.

12. Gesit G, Nandakumar K, Chuang KT. CFD modeling of flow patterns and hydraulics of commercial-scale sieve trays. *AIChE J.* 2003;49(4):910-924.

13. Hirschberg S, Wijn E, Wehrli M. Simulating the two phase flow on column trays. *Chem Eng Res Des.* 2005;83(12):1410-1424.

14. Van Baten J, Krishna R. Modelling sieve tray hydraulics using computational fluid dynamics. *Chem Eng J.* 2000;77(3):143-151.

15. Schultes M. Research on mass transfer columns: passé? *Chem Eng Technol.* 2013;36(9):1539-1549.

16. Hofhuis PAM. *Flow regimes on sieve-trays for gas/liquid contacting*, Technische Hogeschool Delft; 1980.

17. Bernard J, Sargent R. The hydrodynamic performance of a sieve plate distillation column. *Trans Instn Chem Engr.* 1966;44:314-327.

18. Raper JA, Kearney M, Burgess J, Fell C. The structure of industrial sieve tray froths. *Chem Eng Sci.* 1982;37(4):501-506.

19. Pinczewski W, Fell C. Nature of the two-phase dispersion on sieve plates operating in the spray regime. *Trans Inst Chem Eng.* 1974;52(3):294-299.

20. Val Pinczewski W, Benke ND, Fell CJ. Phase inversion on sieve trays. *AlChE J.* 1975;21(6):1210-1213.

21. D'Arcy D. *Analysis of sieve tray froths such as occur in heavy water production plants.* Canada1978. AECL-5828.

22. Jaafar A. Gamma ray scanning for troubleshooting, optimization and predictive maintenance of distillation columns. *Hydrocarbon Asia.* 2005:62-65.

23. Haraguchi MI, Calvo WAP, Kim HY. Tomographic 2-D gamma scanning for industrial process troubleshooting. *Flow Meas Instrum.* 2018;62:235-245.

24. Aquino DD, Mallillin JP, Sulit RF, Hila FC, Nuñez IAA, Bulos AD. Performance evaluation of a rectifier column using gamma column scanning. *Nukleonika.* 2017;62(4):285-287.

25. Gorak A, Schoenmakers H. *Distillation: operation and applications.* Academic Press; 2014.

26. Bell RL. Residence time and fluid mixing on commercial scale sieve trays. *AIChE Journal.* 1972;18(3):498-505.

27. Porter KE, Lockett MJ, Lim CT. The effect of liquid channeling on distillation plate efficiency. *Trans Inst Chem Eng.* 1972;50(2):91-101.

28. Li Y, Wang L, Yao K. New technique for measuring fluid flow patterns on a multiple downcomer tray. *Ind Eng Chem Res.* 2007;46(9):2892-2897.

29. Solari RB, Bell RL. Fluid flow patterns and velocity distribution on commercial-scale sieve trays. *AIChE J.* 1986;32(4):640-649.

30. Yu KT, Huang J, Li JL, Song HH. Two-dimensional flow and eddy diffusion on a sieve tray. *Chem Eng Sci.* 1990;45(9):2901-2906.

31. Schubert M, Piechotta M, Beyer M, Schleicher E, Hampel U, Paschold J. An imaging technique for characterization of fluid flow pattern on industrial-scale column sieve trays. *Chem Eng Res Des.* 2016;111:138-146.

32. Stichlmair J, Ulbrich S. Liquid channelling on trays and its effect on plate efficiency. *Chem Eng Technol.* 1987;10(1):33-37.

33. Biddulph MW, Bultitude DP. Flow characteristics of a small-hole sieve tray. *AIChE J.* 1990;36(12):1913-1916.

34. Porter KE, Yu KT, Chambers S, Zhang MQ. Flow patterns and temperature profiles on a 2.44 m diameter sieve tray. *Chem Eng Res Des.* 1992;70(A):489-500.

35. Liu C, Yuan X, Yu KT, Zhu X. A fluid–dynamic model for flow pattern on a distillation tray. *Chem Eng Sci.* 2000;55(12):2287-2294.

36. Vishwakarma V, Schleicher E, Bieberle A, Schubert M, Hampel U. Advanced flow profiler for two-phase flow imaging on distillation trays. *Chem Eng Sci.* 2021;231.

37. Vishwakarma V, Schleicher E, Schubert M, Tschofen M, Löschau M, Inventors; Helmholtz Zentrum Dresden Rossendorf eV, assignee. Sensor zur Vermessung von Strömungsprofilen in großen Kolonnen und Apparaten. US patent DE1020181245012020.

38. Hampel U, Schubert M, Döß A, et al. Recent advances in experimental techniques for flow and mass transfer analyses in thermal separation systems. *Chem Ing Tech.* 2020;92(7):926–948.

39. Vishwakarma V, Wiedemann P, Schleicher E, Schubert M, Hampel U. A new approach for estimating the effective froth height on column trays. *Chem Eng Sci.* 2021;231.

40. Bennett D, Agrawal R, Cook P. New pressure drop correlation for sieve tray distillation columns. *AlChE J.* 1983;29(3):434-442.

41. Lockett MJ, Kirkpatrick RD, Uddin MS. Froth regime point efficiency for gas-film controlled mass transfer on a two-dimensional sieve tray. *Trans Inst Chem Eng.* 1979;57(1):25-34.

42. Bennett DL, Kao AS, Wong LW. A mechanistic analysis of sieve tray froth height and entrainment. *AlChE J.* 1995;41(9):2067-2082.

43. Garcia JA, Fair JR. A fundamental model for the prediction of distillation sieve tray efficiency. 2. Model development and validation. *Ind Eng Chem Res.* 2000;39(6):1818-1825.

44. Chanson H. Phase-detection measurements in free-surface turbulent shear flows. *J Geophys Eng.* 2016;13(2):S74-S87.

45. Prasser H-M, Böttger A, Zschau J, Gocht T. Needle shaped conductivity probes with integrated micro-thermocouple and their application in rapid condensation experiments with non-condensable gases. *Kerntechnik (1987).* 2003;68(3):114-120.

46. Walton N. Electrical conductivity and total dissolved solids—what is their precise relationship? *Desalination.* 1989;72(3):275-292.

47. Bell RL. Experimental determination of residence time distributions on commercial scale distillation trays using a fiber optic technique. *AlChE J.* 1972;18(3):491-497.

48. Vishwakarma V, Schubert M, Hampel U. Development of a refined RTD-based efficiency prediction model for cross-flow trays. *Ind Eng Chem Res.* 2019;58(8):3258-3268.

49. Vishwakarma V, Schleicher E, Schubert M, Hampel U. Hydrodynamic data of an operational single-pass cross-flow sieve tray [Data set]. In: Rodare, ed2021.

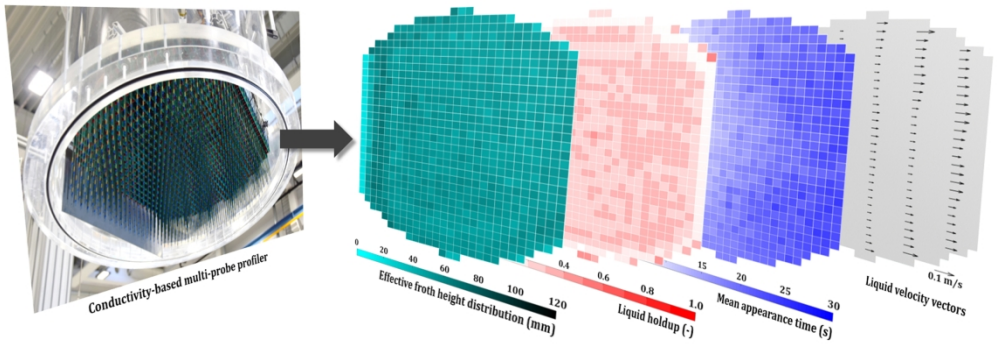

Graphical abstract

338x117mm (300 x 300 DPI)